Robust Stability Analysis of DC Microgrids

Saúl R. Méndez-Elizondo, Jorge A. Morales-Saldaña, and Iván A. Reyes-Portillo

***Abstract*—Direct current (DC) microgrids integrate renewable energy sources, energy storage systems, and electronic loads in order to improve efficiency and flexibility in energy management. However, their stability can be compromised by dynamic interactions among subsystems under different operating conditions, particularly in the presence of constant power loads (CPLs). This paper proposes a robust stability analysis based on the μ-analysis framework. The main contribution is a systematic and reproducible μ-analysis procedure that quantifies robust stability margins under simultaneous load uncertainties applied to DC microgrids. To demonstrate its applicability, a microgrid architecture composed of a high-order Quadratic Buck converter with reduced redundant power processing interacting with a conventional Boost converter is analyzed. Validation is carried out using switched models implemented in the PowerSim simulator under time-varying load conditions. In addition, Monte Carlo simulations are performed by sampling the load parameters to evaluate robustness under simultaneous load uncertainties. The results confirm the effectiveness of the proposed methodology for validating time-domain behavior and assessing robust stability in DC microgrids with CPLs.**

Link to graphical and video abstracts, and to code:
https://latamt.ieeer9.org/index.php/transactions/article/view/10458

***Index Terms*—DC microgrids, Droop control, Modeling, Quadratic Buck, Robust stability, μ-analysis**

I. Introduction

DIRECT CURRENT (DC) microgrids have emerged as an efficient and flexible alternative for integrating renewable sources, energy storage, and electronic loads [1]–[3]. Compared to AC microgrids, they offer greater efficiency, less control complexity, and compatibility with distributed generation. These characteristics have increased their application in data centers, electric mobility, and other systems [4], [5].

In DC microgrids, dynamic interactions between sources and loads can induce instability [6]. For instance, constant power loads (CPLs) exhibit negative incremental resistance (NIR) behavior, which can degrade system damping and stability margins [7]. Moreover, since the operating point and effective load and network parameters may change with loading conditions and tolerances, stability margins are often required beyond a single nominal equilibrium [8].

Stability assessment therefore requires a suitable system representation as the basis for analysis [9], [10]. In this context, DC systems are commonly modeled either in the state-space domain or in the frequency domain. Frequency domain methods use impedance or network equivalents to apply classical stability criteria and loop interpretations, but they require equivalent impedance characterizations for the subsystems [12], [13]. State-space formulations capture converter and controller dynamics and provide a systematic basis to assemble multi-converter models, at the expense of higher-order aggregated descriptions as the architecture grows [14], [15]. In addition, state-space representations enable a structured interconnection of subsystems through explicit input-output interfaces, allowing the systematic assembly of complex microgrid architectures from modular components. When required, state-space models can be extended to frequency and large-signal analysis [16]–[18]. This representation facilitates the preservation of subsystem interconnection structure, which is leveraged in this work to define uncertainty directly at the parameter level within an interconnected framework.

Robust stability analysis evaluates whether the closed-loop system remains stable under admissible parameter changes and quantifies the corresponding stability margins. In terms of robust stability, μ-analysis with structured uncertainty has been adopted to quantify robustness margins under parametric uncertainties in power electronic converters [19]. In [20], structured μ-analysis is used to assess robust stability of a droop-based distributed control scheme, where uncertainties are represented in the frequency domain through multiplicative descriptions. Similarly, in [21], robustness is analyzed using an impedance-based formulation with a frequency-domain uncertainty representation. In these approaches, uncertainty is typically represented in an aggregated or frequency-domain form. Consequently, robustness margins are defined with respect to the chosen representation, making their direct interpretation in terms of individual physical parameters difficult and typically introducing a higher level of conservatism compared to structured parametric representations. Alternative works address robustness through equilibrium analysis and sufficient conditions for equilibrium existence and local stability, derived from nonlinear formulations and small-signal models [22]. Polytopic and LMI-based formulations have also been proposed to assess robust stability under load uncertainty, providing certified bounds on admissible variations [8], [15]. Therefore, a research gap remains regarding the lack of systematic procedures to extract exact robustness margins for simultaneous parameter variations, overcoming the conservative bounds of generalized uncertainty sets. Furthermore, while complementary approaches focus on controller synthesis under CPL uncertainties [23], precise robustness analysis frameworks for existing microgrid architectures are still needed.

In this context, this paper presents a robust stability as-

The associate editor coordinating the review of this manuscript and approving it for publication was Adriana Vargas Martínez (*Corresponding author: Saúl Rolando Méndez Elizondo*).

This work was supported by the Secretaría de Ciencia, Humanidades, Tecnología e Innovación (SECIHTI), Mexico.

Saúl Rolando Méndez Elizondo and J. A. Morales-Saldaña are with the Universidad Autónoma de San Luis Potosí, San Luis Potosí, Mexico (e-mails: saul.mendez@uaslp.mx, and jmorales@uaslp.mx).

I. A. Reyes-Portillo is with the Universidad Autónoma de Zacatecas, Zacatecas, Mexico (e-mail: ivan.reyes@upslp.edu.mx).

sessment based on μ-analysis for DC microgrids, where uncertainty is represented directly in terms of physical parameters within a structured state-space framework. The main methodological contribution is a systematic procedure that extracts an explicit $M-\Delta$ representation using state space port closures. This allows the exact quantification of robust stability margins under simultaneous load uncertainties. Quantitatively, this method defines an exact safety hypercube in the parameter space, providing a strict robustness certificate that maps directly to the physical components.

The proposed approach is demonstrated on a DC microgrid comprising two source converters, a Buck R2P2 and a Boost stage operating under droop control, supplying a resistive load and a constant power load (CPL), demonstrating the applicability of the proposed framework to converter configurations beyond commonly studied topologies. The analysis is conducted on averaged models and validated through time-domain simulations and Monte Carlo tests, comparing the results with the corresponding robustness margins.

The structure of the paper is as follows: Section II describes the modeling and general analysis framework; Section III presents the case study and the robust stability formulation; Section IV shows the results and simulations; Section V presents the discussion; and Section VI presents the conclusions.

II. Modeling of DC Microgrid

Fig. 1 shows the diagram of the DC microgrid analyzed: a set of N source converters connected in parallel to the DC bus via resistors r_k, a bus capacitor C_{bus}, and a set of N_L loads. The diagram shows the main variables: $v_{c,k}$, output voltage of each converter; $i_{o,k}$, injected current into the bus by each source; and i_c, current associated with the bus capacitor. These variables form the basis for the representation of the source subsystem.

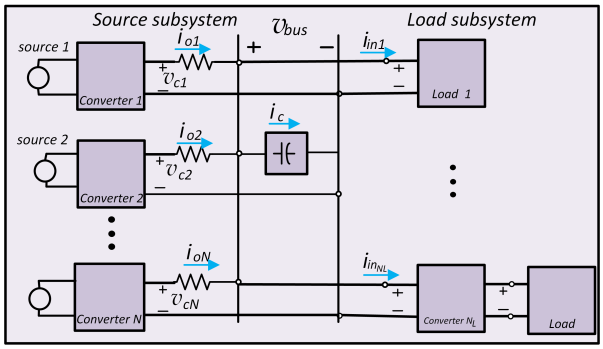

Fig. 1. DC microgrid diagram showing N source converters and N_L loads connected to a common bus via line resistances r_k.

A. Source Subsystem Σ_f

a) Converter-level Modeling: Each source converter is first represented as an independent averaged subsystem $\Sigma_{F,k}$ exposing an output port $(v_{c,k}, i_{o,k})$, where $v_{c,k}$ denotes the converter output-capacitor node voltage and $i_{o,k}$ is defined positive from the converter to the bus network. A generic state-space description is as follows:

$$\Sigma_{F,k}: \begin{cases} \dot{x}_{F,k} = A_{F,k}x_{F,k} + B_{F,k}u_{F,k} + B_{F,k,i}i_{o,k} \\ y^{\text{ext}}_{F,k} = C_{F,k}x_{F,k} + D_{F,k}u_{F,k} + D_{F,k,i}i_{o,k} \\ v_{c,k} = C_{F,k,v}x_{F,k} + D_{F,k,v}u_{F,k} + D_{F,k,vi}i_{o,k} \end{cases} \tag{1}$$

where $x_{F,k} \in \mathbb{R}^{n_{F,k}}$, $u_{F,k} \in \mathbb{R}^{m_{F,k}}$, $y^{\text{ext}}_{F,k} \in \mathbb{R}^{p_{F,k}}$, and $v_{c,k}, i_{o,k} \in \mathbb{R}$. All matrices have compatible dimensions. Here, $y^{\text{ext}}_{F,k}$ collects the converter variables of interest (e.g., input/output currents and output voltage) used for interconnection and analysis, while $C_{F,k,v} \in \mathbb{R}^{1\times n_{F,k}}$ selects the port voltage $v_{c,k}$.

b) Structured Interconnection: The converters are connected to the bus through line resistances r_k by enforcing the port closure:

$$i_{o,k} = \frac{v_{c,k} - v_{\text{bus}}}{r_k}, \qquad k = 1, \ldots, N \tag{2}$$

so that r_k enters only at the assembly stage, consistently with the bus-capacitor dynamics below.

Applying Kirchhoff's current law, the dynamics of the bus capacitor are determined as follows:

$$C_{\text{bus}}\frac{dv_{\text{bus}}}{dt} = \sum_{k=1}^{N}\frac{v_{c,k} - v_{\text{bus}}}{r_k} - i \tag{3}$$

where i is the total current absorbed by the load subsystem, defined as:

$$i = \sum_{j=1}^{N_{\text{L}}} i_{\text{in},j} \tag{4}$$

The state-space model Σ_f of the source subsystem is given as follows:

$$\Sigma_f: \begin{cases} \dot{x}_f = A_f x_f + B_{f,u}u_f + B_{f,i}i \\ y^{\text{ext}}_f = C_{f,y}x_f + D_{f,yu}u_f + D_{f,yi}i \\ v_{\text{bus}} = C_{f,v}x_f + D_{f,vu}u_f + D_{f,vi}i \end{cases} \tag{5}$$

where $x_f \in \mathbb{R}^{n_f}$ is the state vector, $u_f \in \mathbb{R}^{m_f}$ denotes the exogenous inputs (control and disturbances), $y^{\text{ext}}_f \in \mathbb{R}^{p_f}$ denotes the outputs of interest, and i, $v_{\text{bus}} \in \mathbb{R}$, with compatible matrix dimensions. The explicit port closure in (2) and the assembly of the aggregated matrices $A_f, B_{f,u}, B_{f,i}, C_{f,y}, D_{f,yu}, D_{f,yi}, C_{f,v}$ follow directly from the converter-level models (1) and are detailed for the study case in Sec. III.

B. Load Subsystem Σ_ℓ

The load subsystem consists of a set of N_{L} loads (converters and/or passive elements) that consume power from the DC bus. Each load j is modeled independently, and their interaction is established through the shared bus voltage v_{bus}.

From the bus perspective, the load subsystem defines the port relation $v_{\text{bus}} \mapsto i$, i.e., the bus voltage acts as the interconnection input and the total absorbed current i is the corresponding interconnection output.

The state-space model Σ_ℓ of the load subsystem is expressed in (6) as:

$$\Sigma_\ell : \begin{cases} \dot{x}_\ell = A_\ell x_\ell + B_{\ell,u} u_\ell + B_{\ell,v} v_{\text{bus}} \\ i = C_{\ell,i} x_\ell + D_{\ell,iu} u_\ell + D_{\ell,iv} v_{\text{bus}} \\ y_\ell^{\text{ext}} = C_{\ell,y} x_\ell + D_{\ell,yu} u_\ell + D_{\ell,yv} v_{\text{bus}} \end{cases}, \tag{6}$$

where $x_\ell \in \mathbb{R}^{n_\ell}$ is the set of the states of each load, $u_\ell \in \mathbb{R}^{m_\ell}$ represents the exogenous inputs, and $y_\ell^{\text{ext}} \in \mathbb{R}^{p_\ell}$ denotes the outputs of interest.

The structure of Σ_ℓ is block diagonal, since each load interacts only through v_{bus}; accordingly, $i = \sum_{j=1}^{N_{\text{L}}} i_{\text{in},j}$ denotes the total current absorbed by the load subsystem.

C. General Framework for Robust Analysis

The interconnection of the source and load subsystems is illustrated in Fig. 2. The bus voltage v_{bus} and current i are shared by both subsystems.

a) Augmented Plant: In state space, the plant Σ_p is described by:

$$\Sigma_p : \begin{cases} \dot{x}_p = A_p x_p + B_{p,u} u_p + B_{p,d} d \\ y_p^{\text{ext}} = C_{p,\text{e}} x_p + D_{p,\text{e}u} u_p + D_{p,\text{e}d} d \\ y_p = C_{p,y} x_p + D_{p,yu} u_p + D_{p,yd} d \end{cases} \tag{7}$$

where $x_p \in \mathbb{R}^{n_p} = \text{col}(x_f, x_\ell)$ collects the source and load states, $u_p \in \mathbb{R}^{m_f}$ denotes the exogenous inputs, $d \in \mathbb{R}^{m_d}$ represents the control signals of both subsystems, $y_p \in \mathbb{R}^{p_p}$ denotes the plant outputs used for feedback/interconnection, and $y_p^{\text{ext}} \in \mathbb{R}^{p_{\text{ext}}}$ denotes additional plant outputs of interest, with compatible matrix dimensions.

b) Local Controllers: Each converter has an associated local controller K_k, and the set is organized in the diagonal block defined as:

$$\Sigma_K = \text{diag}\{K_1, K_2, \ldots, K_N\} \tag{8}$$

In state space, the controller for the system is expressed in a partitioned form as:

$$\Sigma_K : \begin{cases} \dot{x}_K = A_K x_K + B_{K,y} y_p + B_{K,u} u_K \\ d = C_{K,d} x_K + D_{K,dy} y_p + D_{K,du} u_K \\ y_K^{\text{ext}} = C_{K,\text{ext}} x_K + D_{K,\text{ext}y} y_p + D_{K,\text{ext}u} u_K \end{cases} \tag{9}$$

where $x_K \in \mathbb{R}^{n_K}$ is the controller state vector, $u_K \in \mathbb{R}^{m_K}$ denotes additional controller exogenous inputs (e.g., references/disturbances), and $y_K^{\text{ext}} \in \mathbb{R}^{p_K}$ includes additional controller outputs of interest, with compatible matrix dimensions.

c) Closed System: By interconnecting Σ_p with Σ_K, the closed-loop system is obtained as:

$$\Sigma_{cl} : \begin{cases} \dot{x}_{cl} = A_{cl} x_{cl} + B_{cl,w} w + B_{cl,u} u_K \\ y_{cl}^{\text{ext}} = C_{cl,\text{ext}} x_{cl} + D_{cl,\text{ext}w} w + D_{cl,\text{ext}u} u_K \\ y_{cl} = C_{cl} x_{cl} + D_{cl,w} w + D_{cl,u} u_K \end{cases} \tag{10}$$

where $x_{cl} \in \mathbb{R}^{n_p+n_K} = \text{col}(x_p, x_K)$. Fig. 2 shows the interconnection of the plant and the controller. Moreover, the partitioned input–output form of Σ_{cl} preserves an explicit interconnection interface for modular coupling of additional subsystems.

To ensure that the interconnection is well posed, the following condition must be satisfied:

$$\det\big(I - D_{p,yd} D_{K,dy}\big) \neq 0, \ \det\big(I - D_{\ell,iv} D_{f,vi}\big) \neq 0 \tag{11}$$

which ensures that Σ_{cl} is realizable in state space.

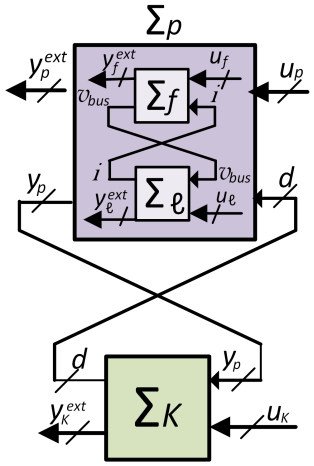

Fig. 2. General interconnection framework showing the coupling of the source and load subsystems to form the plant, and its feedback connection with the controllers.

III. Study Case

Fig. 3 shows the DC microgrid considered as a case study. This is a 48 V single-bus architecture with droop-based current sharing. The source subsystem consists of a quadratic Buck–R2P2 converter [24] that is regulated by a type III compensator with a pole at the origin for local regulation and a Boost converter regulated by a PI controller. The Buck–R2P2 stage is selected for its quadratic conversion gain and reduced redundant power processing, which can improve power-processing efficiency. The Boost stage provides complementary converter dynamics under droop-based current sharing. The load subsystem includes a resistor and a boost converter that operates as a constant power load. The CPL is included as a stressing operating condition to challenge bus regulation and assess the proposed procedure on the overall interconnected system. This case study is also used to illustrate that the proposed port-based assembly is not restricted to conventional buck/boost-type configurations. Nominal operating conditions are summarized in Table I.

TABLE I
Nominal Operating Conditions of the Study Case

Quantity	Value
Bus-voltage setpoint	$V_{\text{bus}}^{\star} = 48$ V
Droop gain	$K_D = 0.16$ V/A
Buck–R2P2 input voltage	$V_{s1} = 120$ V
Source Boost input voltage	$V_{s2} = 24$ V
CPL regulated output voltage	$V_{o2,\text{ref}} = 96$ V
Switching frequency (all converters)	$f_s = 50$ kHz
Nominal bus resistor	$R_{o1,\text{nom}} = 15.36\ \Omega$
CPL emulation resistor	$R_{o2,\text{nom}} = 48\ \Omega$
CPL nominal power	$P_{\text{CPL,nom}} = 192$ W

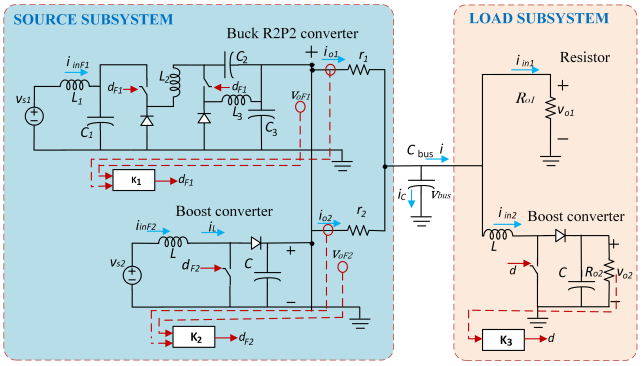

Fig. 3. Schematic of the proposed 48 V DC microgrid study case featuring Buck-R2P2 and Boost converters.

To formulate the state-space representation, the modeling procedure assumes that all converters operate in Continuous Conduction Mode (CCM). The dynamic behavior is described using an averaged modeling approach, neglecting high-frequency switching ripples to focus on the subsystem interactions. Furthermore, the robust stability assessment relies on a linearization around the nominal equilibrium point defined in Table I. Therefore, the computed robustness margins represent a certified stability boundary for the modeled linear dynamics tied to this specific operating condition.

The Buck–R2P2 converter is modeled under this averaged framework, with the state vector defined as follows:

$$\tilde{x}_{F1} = \begin{bmatrix} \tilde{i}_{L1} & \tilde{i}_{L2} & \tilde{i}_{L3} & \tilde{v}_{C1} & \tilde{v}_{C2} & \tilde{v}_{C3} \end{bmatrix}^\top \tag{12}$$

The corresponding input vector is $\tilde{u}_{F1} = [\tilde{v}_{s1}, \tilde{d}_{F1}]^\top$, and the model outputs are the currents and voltages of interest. Here, $\tilde{d}_{F1}$ represents the variation in the duty ratio. Accordingly, the converter small-signal dynamics can be written in state-space form by explicitly exposing the port variables $(\tilde{v}_{c,1}, \tilde{i}_{o1})$, with $\tilde{v}_{c,1} \equiv \tilde{v}_{C3}$, as:

$$\Sigma_{F1} : \begin{cases} \dot{\tilde{x}}_{F1} = A_{F1}\tilde{x}_{F1} + B_{F1}\tilde{u}_{F1} + B_{F1,i}\tilde{i}_{o1} \\ \tilde{y}^{\text{ext}}_{F1} = C_{F1}\tilde{x}_{F1} + D_{F1}\tilde{u}_{F1} + D_{F1,i}\tilde{i}_{o1} \\ \tilde{v}_{c,1} = C_{F1,v}\tilde{x}_{F1} + D_{F1,v}\tilde{u}_{F1} + D_{F1,vi}\tilde{i}_{o1} \end{cases} \tag{13}$$

where $\tilde{i}_{o1}$ is the port current defined positive from the converter to the bus network. The external output vector is selected as:

$$\tilde{y}^{\text{ext}}_{F1} = \begin{bmatrix} \tilde{i}_{\text{in}F1} & \tilde{i}_{o1} & \tilde{v}_{oF1} \end{bmatrix}^\top, \qquad \tilde{v}_{oF1} \equiv \tilde{v}_{c,1} \equiv \tilde{v}_{C3} \tag{14}$$

Similarly, the boost converter is represented by:

$$\tilde{x}_{F2} = \begin{bmatrix} \tilde{i}_L & \tilde{v}_C \end{bmatrix}^\top, \quad \tilde{u}_{F2} = \begin{bmatrix} \tilde{v}_{s2} & \tilde{d}_{F2} \end{bmatrix}^\top \tag{15}$$

and its small-signal dynamics are expressed by exposing the port variables $(\tilde{v}_{c,2}, \tilde{i}_{o2})$, with $\tilde{v}_{c,2} \equiv \tilde{v}_C$, as:

$$\Sigma_{F2} : \begin{cases} \dot{\tilde{x}}_{F2} = A_{F2}\tilde{x}_{F2} + B_{F2}\tilde{u}_{F2} + B_{F2,i}\tilde{i}_{o2} \\ \tilde{y}^{\text{ext}}_{F2} = C_{F2}\tilde{x}_{F2} + D_{F2}\tilde{u}_{F2} + D_{F2,i}\tilde{i}_{o2} \\ \tilde{v}_{c,2} = C_{F2,v}\tilde{x}_{F2} + D_{F2,v}\tilde{u}_{F2} + D_{F2,vi}\tilde{i}_{o2} \end{cases} \tag{16}$$

where $\tilde{i}_{o2}$ is defined positive from the converter to the bus network, and the external output vector is selected as:

$$\tilde{y}^{\text{ext}}_{F2} = \begin{bmatrix} \tilde{i}_{\text{in}F2} & \tilde{i}_{o2} & \tilde{v}_{oF2} \end{bmatrix}^\top \qquad \tilde{v}_{oF2} \equiv \tilde{v}_{c,2} \equiv \tilde{v}_C \tag{17}$$

Structured interconnection (as in Sec. II): the converters are interconnected to the bus by enforcing the port closure:

$$\tilde{i}_{o,k} = \frac{\tilde{v}_{c,k} - \tilde{v}_{\text{bus}}}{r_k}, \qquad k \in \{1, 2\} \tag{18}$$

By substituting these relations into (13)–(16), the local dynamics are rewritten in closed form as:

$$A^\star_{Fk} = A_{Fk} + \frac{1}{r_k} B_{Fk,i} C_{Fk,v}, \qquad k \in \{1, 2\} \tag{19}$$

Following the partitioned framework of Sec. II, the aggregated source subsystem Σ_f is constructed as:

$$\Sigma_f : \begin{cases} \dot{\tilde{x}}_f = A_f\tilde{x}_f + B_{f,u}\tilde{u}_f + B_{f,i}\tilde{i} \\ \tilde{y}^{\text{ext}}_f = C_{f,y}\tilde{x}_f + D_{f,yu}\tilde{u}_f + D_{f,yi}\tilde{i} \\ \tilde{v}_{\text{bus}} = C_{f,v}\tilde{x}_f + D_{f,vu}\tilde{u}_f + D_{f,vi}\tilde{i} \end{cases} \tag{20}$$

where the aggregated state, input, and output vectors are defined as:

$$\tilde{x}_f = \begin{bmatrix} \tilde{x}^\top_{F1} & \tilde{x}^\top_{F2} & \tilde{v}_{\text{bus}} \end{bmatrix}^\top \tag{21a}$$

$$\tilde{u}_f = \begin{bmatrix} \tilde{v}_{s1} & \tilde{d}_{F1} & \tilde{v}_{s2} & \tilde{d}_{F2} \end{bmatrix}^\top \tag{21b}$$

$$\tilde{y}^{\text{ext}}_f = \begin{bmatrix} \tilde{i}_{\text{in}F1} & \tilde{i}_{o1} & \tilde{v}_{oF1} & \tilde{i}_{\text{in}F2} & \tilde{i}_{o2} & \tilde{v}_{oF2} & \tilde{v}_{\text{bus}} \end{bmatrix}^\top \tag{21c}$$

The system matrices exhibit the following block structure:

$$A_f = \begin{bmatrix} A^\star_{F1} & 0 & \alpha_1 \\ 0 & A^\star_{F2} & \alpha_2 \\ \beta_1 & \beta_2 & \gamma \end{bmatrix}, \quad B_{f,u} = \begin{bmatrix} B_{F1} & 0 \\ 0 & B_{F2} \\ 0 & 0 \end{bmatrix}, \quad B_{f,i} = \begin{bmatrix} 0 \\ 0 \\ -\frac{1}{C_{\text{bus}}} \end{bmatrix} \tag{22}$$

where the coupling terms are defined as:

$$\gamma = -\frac{1}{C_{\text{bus}}} \left(\frac{1}{r_1} + \frac{1}{r_2} \right) \tag{23}$$

$$\alpha_k = \frac{1}{r_k} B_{Fk,i}, \quad \beta_k = \frac{1}{r_k C_{\text{bus}}} C_{Fk,v}, \quad k \in \{1, 2\} \tag{24}$$

The load subsystem Σ_ℓ (Eq. 6) is composed of a resistor R_{o1} and a boost converter operated as a constant power load (CPL). Its dynamical model follows the load framework of Sec. II, and the complete matrices are reported in the Appendix.

Accordingly, the total absorbed current seen from the bus is:

$$\tilde{i} = \frac{\tilde{v}_{\text{bus}}}{R_{o1}} + \tilde{i}_{in2}. \tag{25}$$

The open-loop model of the microgrid Σ_p is obtained by interconnecting the source subsystem Σ_f with the load subsystem Σ_ℓ using the Redheffer star product ($\star$) [26], as follows:

$$\Sigma_p = \Sigma_f \star \Sigma_\ell. \tag{26}$$

This interconnection closes the internal variables $(\tilde{v}_{\text{bus}}, \tilde{i})$, yielding an aggregated system Σ_p with external input vector $u_p = [u_f^\top \; u_\ell^\top]^\top$ and external output vector $y^{\text{ext}}_p = [y^{\text{ext}\top}_f \; y^{\text{ext}\top}_\ell]^\top$. The well-posedness condition is satisfied since $D_{f,vi} = 0$ and $D_{\ell,iv} = 0$.

The controllers for the converters are represented by the diagonal structure defined as:

$$\Sigma_K = \text{diag}\{K_1, K_2, K_3\}. \tag{27}$$

For the study case considered in Sec. III, $N = 3$ and the diagonal controller Σ_K reduces to the three local regulators K_1, K_2, and K_3, consistent with the partitioned controller structure defined in (9). Here, K_1 and K_2 correspond to the source-side controllers, while K_3 regulates the load-side converter (CPL). The controller input is given by the plant output vector y_p, whereas the exogenous inputs u_K are set to zero and the auxiliary outputs y_K^{ext} are not used.

The feedback signals are selected from y_p as follows: $K_1 : \mathbb{R}^2 \to \mathbb{R}$ maps $[\,\tilde{i}_{o1},\, \tilde{v}_{oF1}\,]^\top$ to $\tilde{d}_{F1}$, $K_2 : \mathbb{R}^2 \to \mathbb{R}$ maps $[\,\tilde{i}_{o2},\, \tilde{v}_{oF2}\,]^\top$ to $\tilde{d}_{F2}$, and $K_3 : \mathbb{R} \to \mathbb{R}$ maps $\tilde{v}_{o2}$ to the CPL duty-ratio variation $\tilde{d}$. The signals $\tilde{i}_{o1}$ and $\tilde{i}_{o2}$ correspond to the output currents used for droop-based current sharing, while $\tilde{v}_{oF1}$ and $\tilde{v}_{oF2}$ are the output voltages used for inner voltage-mode regulation.

The interconnection between Σ_p and Σ_K defines a lower linear fractional transformation (LFT), where y_p is fed into Σ_K and the resulting control signal d is applied to Σ_p.

The complete closed-loop system is obtained as follows:

$$\Sigma_{cl} = \Sigma_p \star \Sigma_K. \tag{28}$$

The resulting system Σ_{cl} preserves the external interface defined in (10), with $y_{cl}^{\text{ext}} \equiv y_p^{\text{ext}}$. The interconnection is well-posed since the direct feedthrough matrices in the feedback channels are zero, thus avoiding algebraic loops.

M-Δ Formulation

Uncertainty is associated with the load parameters R_{o1} and R_{o2}. Each parameter is modeled as a normalized real perturbation as follows:

$$p_k = \bar{p}_k\,(1 + \alpha_k \delta_k), \qquad \delta_k \in \mathbb{R},\ |\delta_k| \le 1, \tag{29}$$

where $\bar{p}_k$ denotes the nominal value and $\alpha_k \in \mathbb{R}_+$ defines the relative uncertainty level (specifically, $\alpha_1 = \alpha_2 = 0.1$ for a 10% variation). This level reflects standard manufacturing tolerances and typical operating variations in power electronic components. The uncertain closed-loop system is represented in upper linear fractional transformation (LFT) form by:

$$\Sigma_{cl}(\Delta) = \mathcal{F}_u(M, \Delta), \tag{30}$$

where M denotes the nominal interconnection matrix, partitioned as (See Fig. 4):

$$M = \begin{bmatrix} M_{11} & M_{12} \\ M_{21} & M_{22} \end{bmatrix}, \qquad M_{11} \in \mathbb{C}^{r \times r}. \tag{31}$$

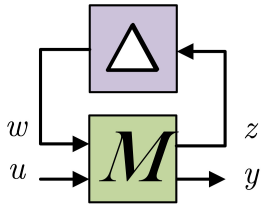

Fig. 4. Standard $M-\Delta$ interconnection framework for robust stability analysis.

The associated signal interconnection is given by:

$$\begin{bmatrix} z \\ y \end{bmatrix} = M \begin{bmatrix} w \\ u \end{bmatrix}, \qquad w = \Delta z, \tag{32}$$

where $z, w \in \mathbb{C}^r$ denote the internal signals in the frequency domain, and u, y represent external inputs and outputs. Due to the high dimensionality caused by repeated parameters across the system realization, the $M - \Delta$ representation is obtained implicitly via standard LFT transformations.

The structure of the uncertainty is defined by the set $\mathbf{\Delta}$, which accounts for the real parametric variations of the load as follows:

$$\mathbf{\Delta} = \{\text{diag}(\delta_1 I_{r_1}, \delta_2 I_{r_2}) : \delta_i \in \mathbb{R}, |\delta_i| \le 1\}, \tag{33}$$

where r_1 and r_2 are the repetition indices of each parameter. Robust stability is assessed using the structured singular value $\mu_\Delta(M_{11}(j\omega))$, defined as:

$$\mu_\Delta(M_{11}(j\omega)) = \frac{1}{\min_{\Delta \in \mathbf{\Delta}} \{\bar{\sigma}(\Delta) : \det(I - M_{11}(j\omega)\Delta) = 0\}}. \tag{34}$$

Since the exact computation of μ_Δ is an NP-hard problem, it is estimated via lower and upper bounds as follows:

$$\underline{\mu}_\Delta(M_{11}(j\omega)) \le \mu_\Delta(M_{11}(j\omega)) \le \overline{\mu}_\Delta(M_{11}(j\omega)). \tag{35}$$

Following the approach in [19], the lower bound ($\underline{\mu}$) is utilized to identify the smallest destabilizing perturbation, providing a direct measure of the actual stability margin, while the upper bound ($\overline{\mu}$) provides a conservative safety certificate.

The frequency-dependent behavior of these bounds is shown in Fig. 5. The computed upper bound satisfies $\overline{\mu}_{\max} \approx 0.429$, yielding a guaranteed robustness margin of $1/\overline{\mu}_{\max} \approx 2.33$. This confirms that the system is robustly stable for the entire 10% uncertainty set. Furthermore, the lower bound satisfies $\underline{\mu}_{\max} \approx 0.134$, indicating a maximum stability margin of $1/\underline{\mu}_{\max} \approx 7.46$.

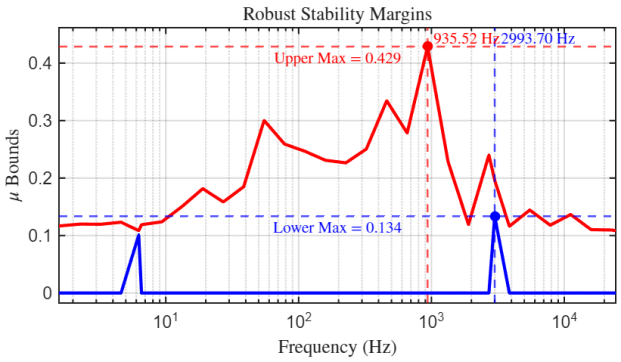

Fig. 5. Structured singular value μ as a function of frequency.

From a physical standpoint, the margin $1/\underline{\mu}_{\max}$ quantifies the maximum simultaneous scaling of the load uncertainties that preserves stability. This stability margin defines a safety hypercube in the parameter space. The independent parameter bounds, derived from the affine mapping between normalized perturbations and physical values, are given by:

$$R_{o1} \in [3.90,\ 26.82]\,\Omega, \qquad R_{o2} \in [12.18,\ 83.82]\,\Omega. \tag{36}$$

The worst-case uncertainty realization is characterized by the perturbation Δ_{des}, obtained from the lower bound algorithm at the critical frequency $\omega^\star$. This yields the parameter combination $R_{o1} \approx 26.82\ \Omega$ and $R_{o2} \approx 13.09\ \Omega$. This asymmetric configuration highlights that instability is driven by the interaction between load parameters rather than their individual extrema. At this condition, the system satisfies $\det(I - M_{11}(j\omega^\star)\Delta_{des}) = 0$, indicating that the closed-loop poles reach the imaginary axis. Finally, since the analysis is based on a linearized model, these results provide a robustness certificate valid for the specific operating point considered.

IV. Simulations and Results

The dynamic response of the interconnected system is analyzed under load variations using simulations. Two scenarios are considered where the values of R_{o1} and R_{o2} change incrementally in successive time intervals. Table II and Fig. 9 summarize the variation profile considered, which matches the case studies evaluated in the simulations shown in Figs. 6 and 7.

TABLE II
VARIATION PROFILE OF R_{o1} AND R_{o2} USED IN TIME-DOMAIN SIMULATIONS

Time (s)	R_{o1} Case 1 (Ω)	R_{o1} Case 2 (Ω)	R_{o2} (Cases 1–2) (Ω)
0.4–0.5	15.36	15.36	48.00
0.5–0.6	12.00	16.00	36.00
0.6–0.7	10.00	17.00	24.00
0.7–0.8	8.00	18.00	20.00
0.8–0.9	6.00	19.00	16.00
0.9–1.0	4.00	20.00	14.00
1.0–1.1	2.50	21.00	12.00
1.1–1.2	1.00	22.00	10.00

Figs. 6 and 7 show the evolution of the bus voltage v_{bus}, the load Boost voltage v_{o2}, and the currents supplied by the Buck–R2P2 and source Boost converters i_{o1} and i_{o2}.

In Case 1, the system remains stable across the variations of R_{o1} and R_{o2} shown in Table II. After $t > 1$ s, a deviation of more than 2 V in the DC bus voltage is observed due to the high current demand.

In Case 2, the bus voltage v_{bus} remains regulated until $t = 1.1$ s. The increase in load causes the system to collapse, as evidenced by the abrupt oscillations of v_{bus}.

Sensitivity Analysis under Individual Parameter Variations: To evaluate the impact of individual parameters, a sensitivity analysis was conducted based on the trace of the dominant closed-loop eigenvalues. Fig. 8 illustrates the movement of the dominant poles when varying R_{o1} within $[4, 30.72]\ \Omega$ while keeping R_{o2} at its nominal value, and subsequently varying R_{o2} within $[12, 96]\ \Omega$ with a nominal R_{o1}. As observed, varying a single parameter across these ranges does not force the dominant poles into the unstable right half-plane, demonstrating that the system remains seemingly stable under isolated variations. Nevertheless, the μ-analysis presented in Section III identified a critical destabilizing point at an asymmetric condition ($R_{o1} \approx 26.82\ \Omega$ and $R_{o2} \approx 13.09\ \Omega$). This confirms that traditional one-dimensional sensitivity approaches

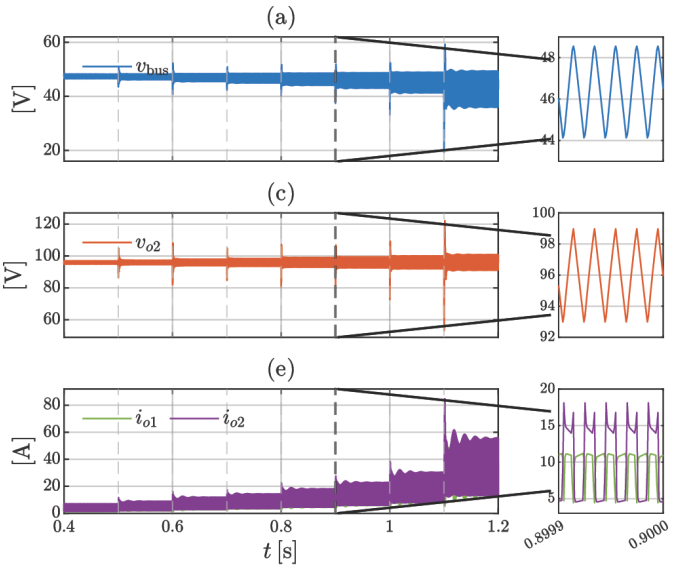

Fig. 6. Transient response of the DC microgrid in Case 1 under the load-variation profile of Table II. The global responses and corresponding zoomed views before 0.9 s are shown for (a) the DC bus voltage v_{bus}, (c) the output voltage v_{o2}, and (e) the output currents i_{o1} and i_{o2}.

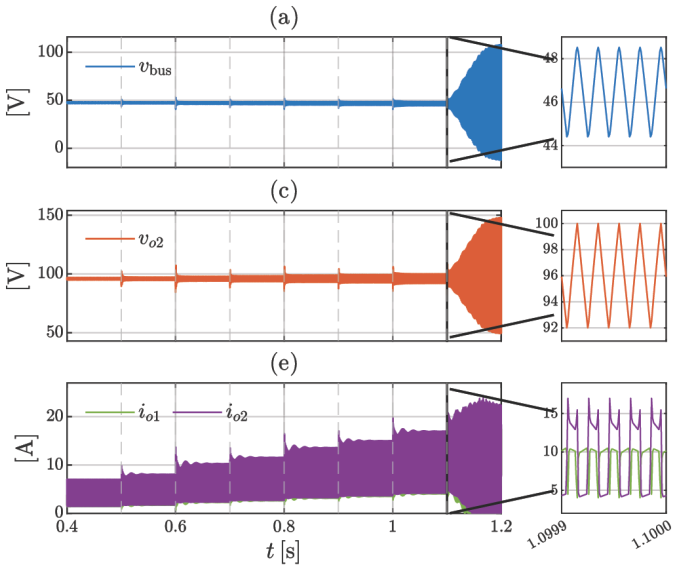

Fig. 7. Transient response of the DC microgrid in Case 2 under the load-variation profile of Table II. The global responses and corresponding zoomed views before 1.1 s are shown for (a) the DC bus voltage v_{bus}, (c) the output voltage v_{o2}, and (e) the output currents i_{o1} and i_{o2}.

yield excessively optimistic stability margins by failing to capture the simultaneous dynamic interactions of multiple loads. Consequently, to explicitly map the actual stability boundaries under simultaneous parameter variations, a Monte Carlo sampling approach is employed to classify the system's behavior across the full parameter space.

Evaluation using Monte Carlo (MC) Simulations: Monte Carlo sampling is employed to explore a large space of simultaneous parameter variations and to complement the robustness prediction obtained through the μ-analysis. For each

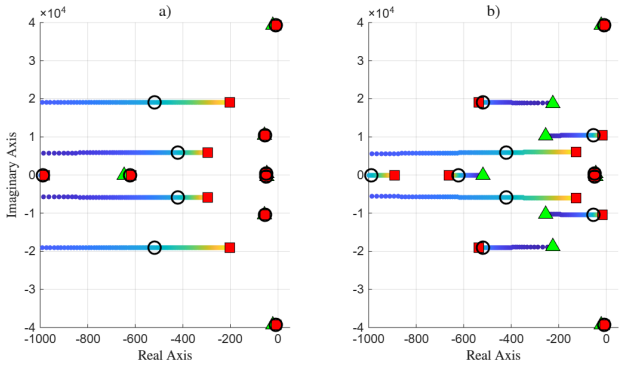

Fig. 8. Dominant eigenvalue traces under individual parameter variations: (a) R_{o1} sweep with nominal R_{o2}; (b) R_{o2} sweep with nominal R_{o1}. Green triangles, red squares, and black circles denote the sweep start, end, and nominal operating points, respectively.

sample, the closed-loop system is evaluated using randomly generated values of the load parameters, and its eigenvalues are computed to assess stability.

A total of 2000 Monte Carlo simulations were performed on the closed-loop system Σ_{cl}, considering random variations in the loads. The exploration ranges were up to $\pm 100\%$ of the nominal values given by:

$$R_{o1} \in (0,\, 30.72]\,\Omega, \qquad R_{o2} \in (0,\, 96]\,\Omega. \tag{37}$$

The eigenvalues of each sampled system were computed and classified into two categories:

- **Stable** (green): all eigenvalues are located in the left half-plane.
- **Unstable** (red): at least one eigenvalue lies in the right half-plane.

Fig. 9 illustrates the Monte Carlo samples within the (R_{o1}, R_{o2}) parameter plane. The black rectangle denotes the stability region derived from the μ-margin (36) for simultaneous variations of both load parameters. These results are further verified through time-domain (TD) simulations in Fig. 6 and Fig. 7, corresponding to the operating points highlighted in blue and pink.

Table III presents the operating points in Table II with the μ-region boundaries and the Monte Carlo stability classification. The table specifies whether each (R_{o1}, R_{o2}) pair resides within the μ-region, alongside the droop-based V_{bus} estimate and total load power P_{load}. In all cases, operating points within the μ-region exhibit stability in both TD and MC simulations. However, results diverge once the system leaves the μ-region: Case 1 remains stable over the reported intervals even at higher loading, whereas Case 2 becomes unstable after $t = 1.1$ s, despite a lower P_{load} than in Case 1. This confirms that the stability boundary is determined by the simultaneous trajectory of (R_{o1}, R_{o2}) rather than the total absorbed power alone.

V. Discussion

The μ-analysis provides a frequency-domain tool to assess robust stability under structured parameter variations. It serves as a framework for the rigorous analysis of already designed systems rather than for controller synthesis. The proposed

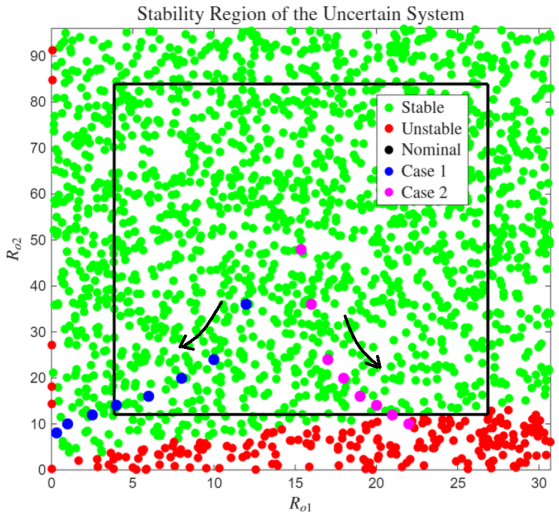

Fig. 9. Stability classification of 2000 samples Monte Carlo simulations based on closed-loop eigenvalues.

TABLE III
Consistency between μ-analysis, Time-domain Simulations, and Monte Carlo Sampling

Time (s)	μ	Case 1			Case 2		
	in/out	V_{bus} (V)	P_{load} (W)	MC	V_{bus} (V)	P_{load} (W)	MC
0.4–0.5	in	47.43	338.5	st	47.43	338.5	st
0.5–0.6	in	47.25	442.1	st	47.33	396.0	st
0.6–0.7	in	46.97	604.6	st	47.13	514.6	st
0.7–0.8	in	46.74	733.9	st	47.01	583.6	st
0.8–0.9	in	46.39	934.6	st	46.82	691.4	st
0.9–1.0	in	45.93	1185.8	st	46.69	767.3	st
1.0–1.1	out	45.19	1585.0	st	46.50	871.0	st
1.1–1.2	out	42.85	2757.8	st	unst	unst	unst

methodology follows a systematic procedure for subsystem modeling, interconnection, and robustness evaluation. Its applicability relies on consistent linearized subsystem models expressed in rational form to construct M–Δ. The analysis is based on a linearized model, which limits the validity of the results to the behavior captured by this representation and does not account for non-idealities or switching effects. The approach is validated through a stability assessment using a high-order converter topology (R2P2 converter) combined with a Boost converter and a CPL load, providing a demanding test case.

The consistency between μ-analysis, Monte Carlo sampling, and time-domain simulations reflects their complementary roles. As quantified in Section IV, while traditional single-parameter sensitivity approaches can yield optimistic margins, μ rigorously identifies worst-case robust stability boundaries under simultaneous parameter variations. Conversely, Monte Carlo and time-domain simulations evaluate specific parameter realizations. To quantify the probabilistic uncertainty of the Monte Carlo method, the 2000 evaluations yield a maximum statistical margin of error of $\pm 2.19\%$ under a 95% confidence interval. In the results, Montecarlo unstable cases concentrate near the μ-based boundary, confirming its interpretation as a critical region mapped with high statistical reliability.

The obtained admissible intervals for (R_{o1}, R_{o2}) define stability margins at the system level and support sensitivity assessment around the considered operating range. However,

the analysis focuses on stability and does not guarantee performance. In particular, droop-controlled microgrids may exhibit voltage deviations under load variations even when stability is preserved.

It is assumed that the proposed methodology could be extended to other architectures involving different types of converters, provided that linear models in rational form are preserved and the interconnection ports are properly defined. However, such an extension may introduce additional modeling and computational complexity. Specifically, scaling the network to include more converters and uncertain parameters increases the dimensions of the Δ matrix, thereby raising the computational cost of the μ bounds calculation, which is left for future research.

VI. Conclusions

This article presents a systematic modeling and analysis methodology for DC microgrids, integrating source and load converters under a generalized robust framework.The study is conducted on averaged CCM models and considers simultaneous parametric variations in the load resistances, defining worst-case robustness conditions.

1) The μ-analysis allows robust stability margins to be quantifiedas a frequency-dependent sufficient guarantee under the adopted M–Δ uncertainty description.
2) The μ-guaranteed region provides a worst-case certificate, while time-domain simulations and Monte Carlo sampling may remain stable beyond this guarantee for specific parameter realizations.
3) The proposed multivariable framework identifies critical asymmetric instability conditions triggered by simultaneous parameter interactions, explicitly demonstrating that traditional linear stability methods are insufficient to detect these worst-case scenarios.

The main contribution of this work is to provide a robust approach that combines classical and robust techniques to assess the stability of DC microgrids. Furthermore, the framework preserves the interconnection structure and internal dynamics of each subsystem.

However, the analysis is limited to linearized averaged models, which do not capture large-signal transients or switching non-idealities. Future work will focus on extending this framework to evaluate robust performance and extrapolating it to assess higher-level control structures in microgrids, alongside model order reduction techniques to improve scalability.

Appendix A
Subsystem Models and Operating Points

This appendix compiles the representation of the state space models used in the modeling section.

A. Converter Models

a) State-space Matrices Buck–R2P2: The state-space matrices for the Buck–R2P2 converter are defined as follows:

$$A_{F1} = \begin{bmatrix} 0 & 0 & 0 & -\frac{1}{L_1} & 0 & 0 \\ 0 & 0 & 0 & \frac{D}{L_2} & -\frac{1}{L_2} & -\frac{1}{L_2} \\ 0 & 0 & 0 & 0 & \frac{D}{L_3} & -\frac{1-D}{L_3} \\ \frac{1}{C_1} & -\frac{D}{C_1} & 0 & 0 & 0 & 0 \\ 0 & \frac{1}{C_2} & -\frac{D}{C_2} & 0 & 0 & 0 \\ 0 & 0 & \frac{1-D}{C_3} & 0 & 0 & 0 \end{bmatrix}, \quad (38)$$

$$B_{F1} = \begin{bmatrix} \frac{1}{L_1} & 0 \\ 0 & \frac{V_{C1}}{L_2} \\ 0 & \frac{V_{C2}+V_{C3}}{L_3} \\ 0 & -\frac{I_{L2}}{C_1} \\ 0 & -\frac{I_{L3}}{C_2} \\ 0 & -\frac{I_{L3}}{C_3} \end{bmatrix}, \quad C_{F1} = \begin{bmatrix} 1 & 0 & 0 & 0 & 0 & 0 \\ 0 & 0 & 0 & 0 & 0 & 0 \\ 0 & 0 & 0 & 0 & 0 & 1 \end{bmatrix}, \quad (39)$$

$$B_{F1,i} = \begin{bmatrix} 0 \\ 0 \\ 0 \\ 0 \\ 0 \\ -\frac{1}{C_3} \end{bmatrix}, \qquad D_{F1,i} = \begin{bmatrix} 0 \\ 1 \\ 0 \end{bmatrix}. \quad (40)$$

b) State-space Matrices Boost: Similarly, the system matrices for the source boost converter are given by:

$$A_{F2} = \begin{bmatrix} 0 & -\frac{1-D}{L} \\ \frac{1-D}{C} & 0 \end{bmatrix}, \qquad B_{F2} = \begin{bmatrix} \frac{1}{L} & \frac{V_C}{L} \\ 0 & -\frac{I_L}{C} \end{bmatrix}, \quad (41)$$

$$C_{F2} = \begin{bmatrix} 1 & 0 \\ 0 & 0 \\ 0 & 1 \end{bmatrix}, \qquad B_{F2,i} = \begin{bmatrix} 0 \\ -\frac{1}{C} \end{bmatrix}, \qquad D_{F2,i} = \begin{bmatrix} 0 \\ 1 \\ 0 \end{bmatrix}. \quad (42)$$

B. Boost Converter (Load Subsystem)

a) States, Inputs and Outputs: For the boost converter operating as a load, the state, input, and output vectors are defined as:

$$\tilde{x} = \begin{bmatrix} \tilde{i}_L & \tilde{v}_C \end{bmatrix}^\top, \quad \tilde{u} = \begin{bmatrix} \tilde{v}_{\text{bus}} & \tilde{d} \end{bmatrix}^\top, \quad \tilde{y} = \begin{bmatrix} \tilde{i}_{\text{in2}} & \tilde{v}_{o2} \end{bmatrix}^\top, \quad (43)$$

while the corresponding dynamic matrices are expressed as follows:

$$A = \begin{bmatrix} 0 & -\frac{1-D}{L} \\ \frac{1-D}{C} & -\frac{1}{C\,R_{o2}} \end{bmatrix}, \quad B = \begin{bmatrix} \frac{1}{L} & \frac{V_o}{L} \\ 0 & -\frac{I_L}{C} \end{bmatrix}, C = \begin{bmatrix} 1 & 0 \\ 0 & 1 \end{bmatrix}. \quad (44)$$

C. Load Subsystem Model

The state-space model for the aggregated load subsystem is defined by:

$$\dot{\tilde{x}}_\ell = A_\ell \tilde{x}_\ell + B_\ell \tilde{u}_\ell, \qquad \tilde{y}_\ell = C_\ell \tilde{x}_\ell + D_\ell \tilde{u}_\ell, \quad (45)$$

with $\tilde{x}_\ell = [\,\tilde{i}_L,\, \tilde{v}_C\,]^\top$, $u_\ell = [\,\tilde{v}_{\text{bus}},\, \tilde{d}\,]^\top$, and outputs given as:

$$y_\ell = \begin{bmatrix} \tilde{i}_{\text{in1}} & \tilde{i}_{\text{in2}} & \tilde{i} & \tilde{v}_{o2} \end{bmatrix}^\top, \qquad \tilde{i} = \tilde{i}_{\text{in1}} + \tilde{i}_{\text{in2}}. \quad (46)$$

ACKNOWLEDGMENTS

The authors thank Secretaría de Ciencia, Humanidades, Tecnología e Innovación (SECIHTI).

REFERENCES

[1] F. S. Al-Ismail, "DC microgrid planning, operation, and control: A comprehensive review," *IEEE Access*, vol. 9, pp. 36154–36172, 2021, doi: 10.1109/ACCESS.2021.3062840.

[2] I. A. Reyes-Portillo, S. R. Méndez-Elizondo, J. A. Morales-Saldaña, J. U. Muñoz-Minjares, C. A. Rivera-Romero and D. L. Castro-López, "Analysis and Modeling of a Boost Converter with Power Processing Reduction for PV Applications," in IEEE Latin America Transactions, vol. 24, no. 4, pp. 412-421, April 2026, doi: 10.1109/TLA.2026.11435591.

[3] S. Punitha, N. P. Subramaniam, and P. A. D. Vimal Raj, "A comprehensive review of microgrid challenges in architectures, mitigation approaches, and future directions," *Journal of Electrical Systems and Information Technology*, vol. 11, no. 1, p. 60, 2024, doi: 10.1186/s43067-024-00188-4.

[4] M. Uddin, H. Mo, D. Dong, S. Elsawah, J. Zhu, and J. M. Guerrero, "Microgrids: A review, outstanding issues and future trends," *Energy Strategy Reviews*, vol. 49, p. 101127, 2023, doi: 10.1016/j.esr.2023.101127.

[5] A. W. Adegboyega, S. Sepasi, H. O. R. Howlader, B. Griswold, M. Matsuura, and L. R. Roose, "DC microgrid deployments and challenges: A comprehensive review of academic and corporate implementations," *Energies*, vol. 18, no. 5, p. 1064, 2025, doi: 10.3390/en18051064.

[6] E. Hossain, R. Perez, A. Nasiri, and S. Padmanaban, "A comprehensive review on constant power loads compensation techniques," *IEEE Access*, vol. 6, pp. 33285–33305, 2018, doi: 10.1109/ACCESS.2018.2849065.

[7] M. Anees, H. Tu and S. Lukic, "Stability Considerations for Virtual Capacitor Control in Constant Power DC Loads," in IEEE Transactions on Power Electronics, vol. 40, no. 4, pp. 4734-4739, April 2025, doi: 10.1109/TPEL.2024.3518478.

[8] J. Liu, W. Zhang and G. Rizzoni, "Robust Stability Analysis of DC Microgrids With Constant Power Loads," in IEEE Transactions on Power Systems, vol. 33, no. 1, pp. 851-860, Jan. 2018, doi: 10.1109/TPWRS.2017.2697765.

[9] A. Francés, R. Asensi, Ó. García, R. Prieto, and J. Uceda, "Modeling electronic power converters in smart DC microgrids—An overview," *IEEE Transactions on Smart Grid*, vol. 9, no. 6, pp. 6274–6287, 2018, doi: 10.1109/TSG.2017.2707345.

[10] D. Espín-Sarzosa, R. Palma-Behnke, C. A. Cañizares, U. Annakkage, M. Elizondo, E. Espina, W. Du, M. Kabalan, L. Meegahapola, P. A. Mendoza-Araya, E. Nasr, A. Pavani, R. Ramos, M. Ropp, K. P. Schneider, J. W. Simpson-Porco, K. Strunz, G. Taranto, F. Tuffner, and J. T. Reilly, "Microgrid modeling for stability analysis," *IEEE Transactions on Smart Grid*, vol. 15, no. 3, pp. 2459–2479, 2024, doi: 10.1109/TSG.2023.3326063.

[11] R. Krishan and Y. Rohith, "Load and generation converters control strategy to enhance the constant power load stability margin in a DC microgrid," *IEEE Access*, vol. 12, pp. 35972–35983, 2024, doi: 10.1109/ACCESS.2024.3370673.

[12] Q. Ma, Q. Zhang, J. Fang, and X. Liu, "Bus-impedance-based stability improvement of DC power distribution system considering dynamic performance," *International Journal of Electrical Power & Energy Systems*, vol. 155, pt. B, Art. no. 109587, 2024, doi: 10.1016/j.ijepes.2023.109587.

[13] M. Leng, G. Zhou, H. Li, G. Xu, F. Blaabjerg, and T. Dragičević, "Impedance-based stability evaluation for multibus DC microgrid without constraints on subsystems," *IEEE Transactions on Power Electronics*, vol. 37, no. 1, pp. 932–943, 2022, doi: 10.1109/TPEL.2021.3093372.

[14] M. Su, Z. Liu, Y. Sun, H. Han, and X. Hou, "Stability analysis and stabilization methods of DC microgrid with multiple parallel-connected DC–DC converters loaded by CPLs," *IEEE Transactions on Smart Grid*, vol. 9, no. 1, pp. 132–142, 2018, doi: 10.1109/TSG.2016.2546551.

[15] M. Carnaghi, P. Cervellini, M. Judewicz, R. Garcia Retegui and M. Funes, "Stability analysis of a Networking DC microgrid with distributed droop control and CPLs," in IEEE Latin America Transactions, vol. 21, no. 9, pp. 966-975, Sept. 2023, doi: 10.1109/TLA.2023.10251802.

[16] W. Xie, M. Han, W. Cao, J. M. Guerrero and J. C. Vasquez, "System-Level Large-Signal Stability Analysis of Droop-Controlled DC Microgrids," in IEEE Transactions on Power Electronics, vol. 36, no. 4, pp. 4224-4236, April 2021, doi: 10.1109/TPEL.2020.3019311.

[17] Z. Zhang, X. Yang, S. Zhao, D. Wu, J. Cao, M. Gao, G. Zeng, and Z. Wang, "Large-signal stability analysis of islanded DC microgrids with multiple types of loads," *International Journal of Electrical Power & Energy Systems*, vol. 143, Art. no. 108450, Dec. 2022, doi: 10.1016/j.ijepes.2022.108450.

[18] L. Ding and C. K. Tse, "Large-signal stability analysis of DC distribution systems with cascading converter structure," *IEEE Transactions on Industrial Electronics*, vol. 70, no. 9, pp. 9103–9111, 2023, doi: 10.1109/TIE.2022.3206692.

[19] S. Sumsurooah, M. Odavic, S. Bozhko, and D. Boroyevich, "Robust stability analysis of a DC/DC buck converter under multiple parametric uncertainties," *IEEE Transactions on Power Electronics*, vol. 33, no. 6, pp. 5426–5441, 2018, doi: 10.1109/TPEL.2017.2736023.

[20] M. Mirjafari, M. Banejad, H. Molla-Ahmadian, A. Sedehi, and F. Blaabjerg, "Robust stability analysis of a novel droop-based distributed control scheme for islanded operation of DC microgrids," *IET Renewable Power Generation*, vol. 16, no. 15, pp. 3325–3338, 2022, doi: 10.1049/rpg2.12585.

[21] S. Méndez-Elizondo, J. Morales-Saldaña, I. Reyes-Portillo, R. Peña-Gallardo, and E. Netzahuatl-Huerta, "Robustness study of a DC nanogrid based on a distributed generation system," in *Proc. 2020 IEEE International Autumn Meeting on Power, Electronics and Computing (ROPEC)*, 2020, pp. 1–6, doi: 10.1109/ROPEC50909.2020.9258740.

[22] Z. Liu and J. Li, "Robust Stability of DC Microgrid Under Distributed Control," in IEEE Access, vol. 10, pp. 97888-97896, 2022, doi: 10.1109/ACCESS.2022.3205615.

[23] E. Moradi-Khaligh, S. Karimi, and M. S. Sadabadi, "Robust LMI-based voltage control strategy for DC microgrids under disturbances and constant power load uncertainties," *Electric Power Systems Research*, vol. 241, Art. no. 111333, 2025, doi: 10.1016/j.epsr.2024.111333.

[24] I. A. Reyes-Portillo, S. R. Méndez-Elizondo, J. A. Morales-Saldaña, C. A. Rivera-Romero, and D. L. Castro-López, "Design of a transformerless DC regulator with reduced redundant power processing for a residential DC microgrid," *IEEE Latin America Transactions*, vol. 23, no. 5, pp. 427–436, 2025, doi: 10.1109/TLA.2025.10974364.

[25] S. R. Méndez-Elizondo, J. A. Morales-Saldaña, I. A. Reyes-Portillo and R. Peña-Gallardo, "Controllability Analysis of a Quadratic Buck Converter with Redundant Power Processing," 2023 IEEE International Autumn Meeting on Power, Electronics and Computing (ROPEC), Ixtapa, Mexico, 2023, pp. 1-6, doi: 10.1109/ROPEC58757.2023.10409481.

[26] K. Zhou and J. C. Doyle, *Essentials of Robust Control*. Upper Saddle River, NJ, USA: Prentice Hall, 1998, vol. 104, doi: 10.1016/S0005-1098(01)00272-2.

Saúl Rolando Méndez-Elizondo received the B.S. degree in biomedical engineering in 2017 and the M.S. degree in electrical engineering in 2020 from the Universidad Autónoma de San Luis Potosí, San Luis Potosí, Mexico. He is currently pursuing the Ph.D. degree in electrical engineering at the Universidad Autónoma de San Luis Potosí. His research interests include DC/DC converters, stability analysis of DC microgrids, energy storage systems, and control design for power electronic systems.

Jorge Alberto Morales-Saldaña received the degree of Electrical Engineer and the degrees of Master´s and Ph.D. degrees in Electrical Engineering from the Universidad Autónoma de San Luis Potosi, San Luis Potosí, Mexico, in 1995, 1997 and 1999, respectively. He currently works at the Faculty of Engineering of the same University as a Research Professor. His main areas of interest are the development of high-efficiency switching converters, DC/DC conversion systems, resonant converters, dynamic analysis of DC power systems, robust analysis, and control engineering applied to power electronic systems.

Iván Alfonso Reyes-Portillo received the degree of Electromechanical Engineer from the Instituto Tecnológico Superior de San Andrés Tuxtla, San Andrés Tuxtla, Veracruz, México in 2016 and the degree of Master of Science in Electronic Engineering from the Centro Nacional de Investigacion y Desarrollo Tecnológico, Cuernavaca, Morelos, México in 2019. Obtained a Ph.D. in Electrical Engineering from the Universidad Autónoma de San Luis Potosí, San Luis Potosí, México, in 2024. He is currently a professor at the Universidad Politecnica de San Luis Potosí, in the Academy of Industrial Systems and Technologies Engineering, and an associate researcher at the Universidad Autónoma de Zacatecas. His main areas of interest are DC/DC converters, redundant power processing converters, energy storage, and renewable energies.